Axion haloscope resonators: The polygonal coaxial cavity

R. Di Vora,* A. Lombardi, A. Ortolan, and G. Ruoso
INFN, Laboratori Nazionali di Legnaro, Legnaro, Padova, Italy

C. Braggio
INFN, Sezione di Padova, Padova, Italy
and Dipartimento di Fisica e Astronomia "G. Galilei", Università di Padova, Padova, Italy

G. Carugno and A. Gardikiotis
INFN, Sezione di Padova, Padova, Italy

(Received 22 March 2024; revised 5 September 2024; accepted 6 February 2025; published 20 March 2025)

In the search for axionic dark matter, the high-frequency part of the quantum chromodynamics (QCD) axion parameter space is favored, as indicated by both cosmological and astrophysical arguments and recent indications from lattice QCD calculations. To extend the probing range of cavity haloscopes, solutions addressing the unfavorable scaling of cavity volume with frequency must be developed. Here, we present a novel type of high-volume thin-shell resonator for high-frequency haloscope dark-matter searches. The cavity is formed by two nested and coaxial right-angled polygonal prisms enclosed within two flat endcaps. For the axion-sensitive (pseudo-)TM_{010} mode at about 10 GHz, finite-element simulations yield a form factor on the order of 0.8 and a Q factor on the order of 60 000 for a copper cavity at 4 K. Reasonable tunability of up to ∼5% is achieved by reciprocal rotation of the two prisms, without relevant changes in haloscope sensitivity. A prototype aluminum hexagonal cavity was built and tested, confirming the main characteristics of the design.

DOI: 10.1103/PhysRevApplied.23.034047

I. INTRODUCTION

The axion is a pseudo-Goldstone boson introduced by Weinberg [1] and Wilczek [2] as part of the Peccei-Quinn mechanism to solve the Standard Model puzzle known as the strong-CP problem of quantum chromodynamics (QCD) [3,4]. In current axion models, the QCD axion would have low mass and very weak interaction with ordinary matter. Additionally, cosmological axions created during the Peccei-Quinn phase transition would be nonrelativistic and have decay times much longer than the age of the Universe, making such "invisible" axions ideal candidates for the composition of dark matter. Astrophysical bounds and cosmological considerations select a range of $1\ \mu\text{eV} < m_a < 10$ meV [5–7] for postinflationary axions, with recent lattice QCD calculations favoring the 40–180 μeV region [8].

In the last few years, increasing efforts have been invested into the detection of the axion as the possible majority constituent of cold dark matter, with a large portion of the experiments employing the axion haloscope originally proposed by Sikivie [9]. In its simplest form, this experimental scheme exploits the large temporal (and spatial) coherence of the axion field by collecting the power released in a microwave resonator immersed in a strong magnetic field.

The converted axion power is (in the limit $Q_0 \ll Q_a$, with $Q_a \sim 1.2 \times 10^6$ the equivalent quality factor of the virialized axion in Earth's reference frame [10,11])

$$P_a = g_{a\gamma\gamma}^2 \frac{\rho_a}{m_a^2} \omega_c B_0^2 C V Q_0 \frac{\beta}{(1+\beta)^2}, \tag{1}$$

where $g_{a\gamma\gamma}$ is the axion-to-photon effective coupling, $\rho_a \sim 0.45\ \text{GeV/cm}^3$ is the axion density [6], m_a is the axion mass, ω_c is the cavity frequency, B_0 is the employed static magnetic field, Q_0 is the unloaded quality factor of the cavity mode, and β is the coupling coefficient of the antenna to the cavity mode. The form factor C expresses the overlap between the electric field $\mathbf{E}_{mnl}(\vec{x})$ of the employed cavity mode and the external magnetic field $\mathbf{B}(\vec{x})$ enabling the axion-to-photon conversion. It is given by

$$C = \frac{|\int_V \mathbf{E}_{mnl} \cdot \mathbf{B}\, \mathrm{d}^3x|^2}{\int_V |\mathbf{B}|^2\, \mathrm{d}^3x \int_V \epsilon |\mathbf{E}_{mnl}|^2\, \mathrm{d}^3x}, \tag{2}$$

where $\epsilon(\vec{x})$ is the dielectric constant at every point $\vec{x}$ in the cavity volume V. In the following, we will assume $\mathbf{B}(\vec{x}) = B_0\hat{\mathbf{z}}$.

Since the axion frequency is to date unknown, an axion haloscope must be able to tune its resonator to cover a

*Contact author: divora@lnl.infn.it

range of frequencies. The speed at which this range can be scanned at a certain level of sensitivity in $g_{a\gamma\gamma}$ is called the haloscope scan rate [12]. It is directly proportional to the so-called "figure of merit" F, which collects all the cavity-related parameters

$$F = (CV)^2 Q_0, \tag{3}$$

the most useful quantity in the design of a new cavity.

Solenoids are the common source of high-intensity magnetic fields. For a given coil length, the available volume scales with the squared radius of the bore. Assuming the use of a cylindrical empty cavity as the resonator, the figure of merit is maximized by its fundamental mode TM_{010}, whose resonant frequency is set by the inverse of the diameter of the cavity. An increase in the targeted mass then automatically results in a quadratic reduction of the volume of the cavity. The haloscope approach is then extremely effective towards the lower end of the QCD axion mass search range, with the most sensitive experiments having already been able to probe the theoretically expected couplings [13–20].

To address the unfavorable scaling of the signal towards high frequencies, several solutions were put forth to increase the occupation of the magnet bore by substituting the standard empty cylindrical TM_{010} resonator. Among them, notable resonator classes are tunable multirod cavities [21,22], dielectric cavities [23–27], photonic bandgap cavities [28–30], the so-called "plasma haloscope" [31,32], the so-called "pizza cavity," or multicell concepts [33–35], and the use of an array of K cavities [36–40]. The last solution is particularly advantageous when the cavities are coherently read out, as the sensitivity gain is proportional to K, instead of just $\sqrt{K}$ as is the case of incoherent arrays [37,39,40]. However, exploiting coherence becomes increasingly difficult with the number of cavities due to the high accuracy requirements of the mechanical tuning system. The pizza cavity concept instead relies on a single cylindrical cavity filling the available bore, where identical azimuthal slices are separated through conductive diaphragms. This approach, while interesting to maximize the effective volume, leads to a rapid increase of the number of partitions for larger magnet bore radius, further complicating the tuning system. Recently, a new approach has emerged in the form of folded thin-shell cavities [41–43], where a large volume is obtained by folding a sheetlike cavity along one of the dimensions. This solution also allows for very wide tuning by a very precise variation of the shells' separation.

In this work we introduce a new, widely and easily tunable high-volume resonator for high-frequency dark-matter haloscopes. It is based on two nested, polygonal coaxial prisms enclosed within two flat endcaps. This design represents a decisive improvement on the standard TM_{010} empty cylindrical cavity paradigm and exploits what we think is the most simple and robust tuning system possible, i.e., rigid rotation around a single, fixed axis.

In Sec. II, we describe the cavity design and its fundamental characteristics. Section II A details the results of the simulation evaluating the cavity tuning range and the stability of the cavity parameters over this range. We show that, as a consequence of the trade-off between tuning range and effective volume, once operational frequency and external diameter are chosen, there exists an optimal choice of cavity design for each desired tuning range. In Sec. II B we present the results of indicative studies on the influence on the cavity parameters of nonidealities in the cavity geometry, leading to the determination of the maximum allowable tolerances. Experimental results obtained for a full-scale prototype of the cavity are detailed in Sec. III. In Sec. IV the projected sensitivity of the studied approach is then compared to the benchmarks provided by pizza cavities and cavity arrays. Finally, in Sec. V we briefly recap the obtained results and draw our conclusions.

II. THE TUNABLE POLYGONAL RESONATOR

In designing the cavity subject of this work, we first considered a thin-shell cavity delimited by two nested coaxial and concentric cylinders of equal height and flat endcaps. The radii of the two cylinders are r_{in} and r_{ext}, respectively (with $r_{\text{in}} < r_{\text{ext}}$). Given the cavity length L, we choose a gap $d = r_{\text{ext}} - r_{\text{in}} \ll \{L, r_{\text{in}}\}$. The properties of such a cavity are easily derived in the limit of large inner radius and infinite sides, where it simplifies to an infinite rectangular box. The gap width d sets the frequency of the TM_{010} mode of such a cavity, which has a very high form factor of $\sim$0.81, as reported in Ref. [41]. The TM_{010} mode of the cylindrical design maintains azimuthal and longitudinal uniform radial field profiles; thus C and Q values close to those of the TM_{010} mode of the infinite rectangular limit cavity are expected. Since the volume of such a cavity scales as $\lambda(r_{\text{in}} + r_{\text{ext}})/2$ instead of λ^2, with λ the wavelength corresponding to the cavity resonant frequency, it represents an extremely sensitive transducer for QCD axions, especially in the high-frequency region of the parameter space, where typically available solenoids are much wider than λ.

To use this cavity in a haloscope, frequency tuning is necessary. Insertion of conductor or dielectric rods [44] inside the cavity quickly degrades the form factor of the mode, as do any geometrical perturbations that break the cylindrical symmetry of the cavity. The optimal solution is a uniform tuning of the gap width, similarly to what is done in thin-shell cavities, but achieving this in a cylindrical geometry appears challenging. However, by substituting the cylinders with right prisms based on regular polygons with the same number of sides N, the continuous azimuthal symmetry of the system becomes discrete. Thanks to this

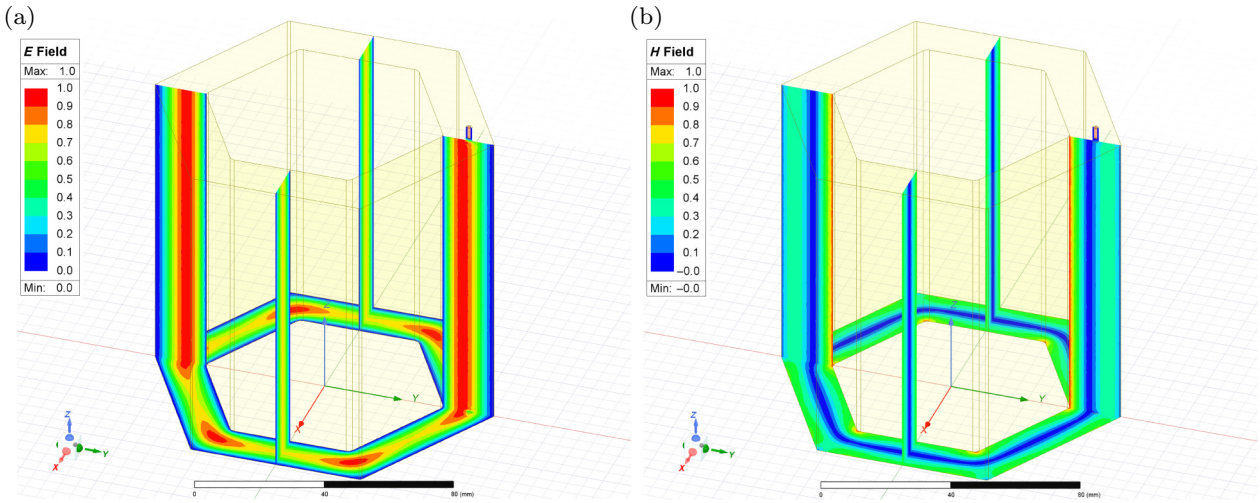

FIG. 1. Basic cavity model used for simulation studies. (a) Electric field and (b) magnetic field distributions as seen from eigenmode simulation. The cavity is an empty region delimited by two solid copper coaxial polygonal prisms and two endcaps. Each endcap hosts a coaxial port used for modal simulations. The auxiliary copper structure enveloping the cavity is not shown in the figure.

symmetry breaking, the azimuthal field distributions and resonant frequency of the transverse modes depend on the reciprocal angle between the two prisms. By simply rotating one prism with respect to the other, we can tune the cavity resonant frequency without excessively impacting the quality factor and the form factor of the mode.

For the present cavity design, the two nested coaxial prisms are enclosed within two flat endcaps. The cavity supports a (pseudo-)TM_{010} axion-sensitive mode between the two prisms as depicted in Fig. 1, where electric and magnetic field distributions are shown. As the cavity has constant section, the field distributions are longitudinally uniform.

A. Cavity frequency tuning

By using a finite-element method (FEM) simulation software package (Ansys HFSS) we study the properties of our resonator. In the cavity model we choose internal and external circumradii $r_{in} = 39.14$ mm and $r_{ext} = 55.92$ mm, respectively. The gap width d sets at first order the resonant frequency, while the number of sides determines the obtainable tuning range. We define an angle ϕ to describe the relative rotation of the two prisms, setting $\phi = 0$ when the prisms have parallel sides. Because of symmetry and cyclicity of the system, ϕ values span the range 0 to $\phi_{max} = \pi/N$. Figure 2 shows the electric field profiles obtained from FEM simulations for different rotation angles. The rotation concentrates the electric field at the external prism

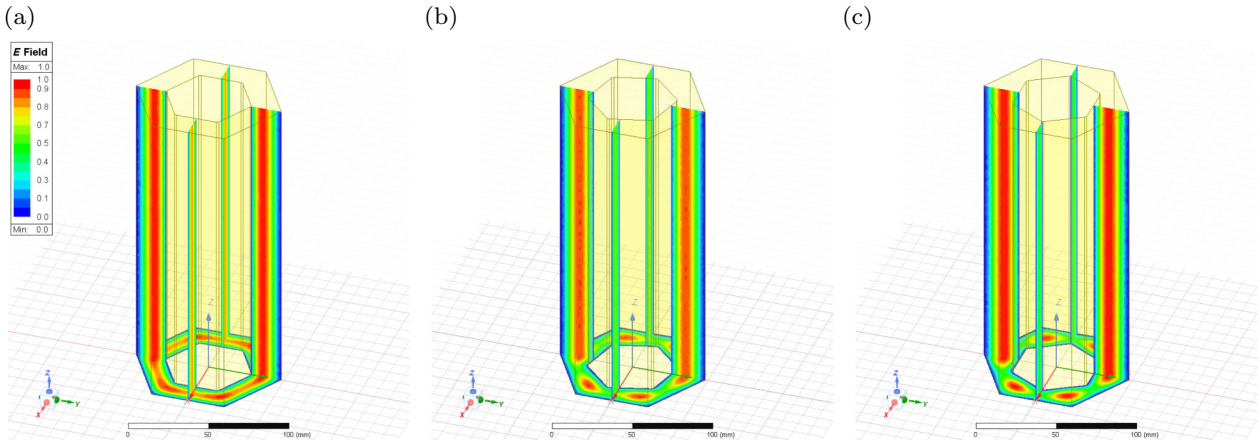

FIG. 2. Electric field profiles obtained from HFSS eigenmode simulation for the TM_{010} mode. Electric field distributions: (a) prisms with no reciprocal rotation; (b) prisms with 15° reciprocal rotation; and (c) prisms with 30° reciprocal rotation. Cavity dimensions were $r_{in} = 39.14$ mm and $r_{ext} = 55.92$ mm for the internal and external circumradii and $L = 210$ mm for the length.

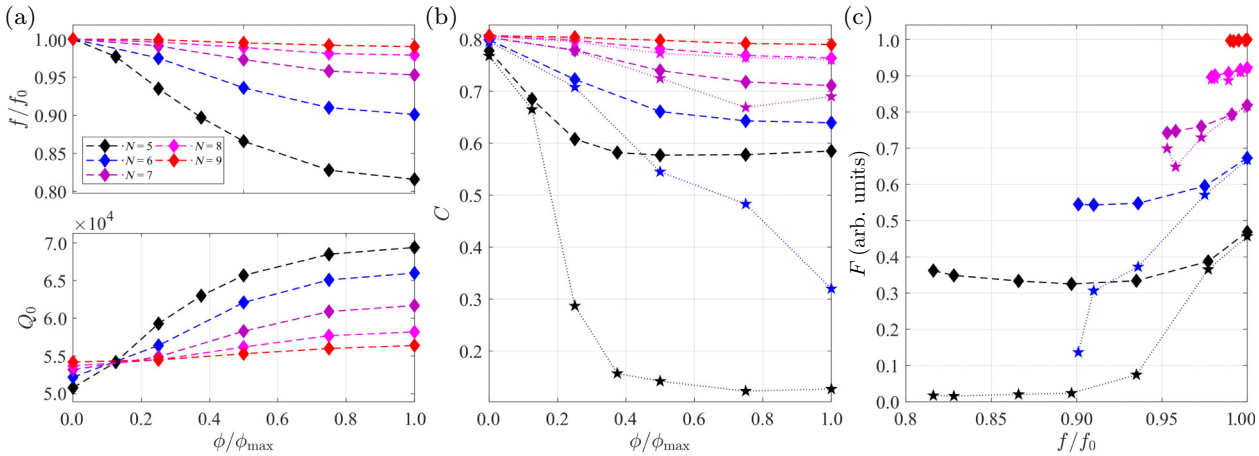

FIG. 3. Internal prism rotation and cavity parameters for various numbers of sides of the polygonal coaxial cavity. All cavity volumes have been renormalized to the same frequency, maintaining constant external radius and assuming inverse linear scaling with the cavity channel width $w = d\cos(\pi/N)$. Compared to the model shown in Fig. 2, we use a 50-mm-long cavity to reduce computational costs. For the driven modal simulations, excitation and readout antenna were placed facing each other on opposite endcaps, positioned at the maximum of the electric field of the cavity when at 0° tuning. Driven modal simulations are plotted with dotted lines, while dashed lines indicate eigenmode simulations. (a) Normalized frequency shift (top) and unloaded quality factor (bottom) versus normalized rotation angle. Here, we plot only eigenmode simulation results since the driven modal ones are essentially identical. (b) Form factor versus normalized rotation angle. (c) Figure of merit as a function of normalized frequency. Note that, when the signal is extracted from a single antenna, the driven modal simulations provide the correct results for the studied parameters. Results of eigenmode simulations hold if a suitable antenna array is employed (see Ref. [45]).

vertexes, increasing the effective width of the cavity and in turn diminishing the cavity frequency.

In Fig. 3 we plot the cavity parameters for polygonal resonators with $N = 5$ to 9 sides, as a function of $\phi/\phi_{\max}$. To reduce computational costs, we used 50-mm-length cavities with the same circumradii as in Fig. 2. Despite the relatively short cavity length, the quality factor Q_0 is dominated by dissipation on the lateral faces. As the cavity wall gap changes with number of sides, the values of the resonant frequency f_0 of the TM_{010} mode at $\phi = 0$ are reported in Table I.

The change of the normalized frequency f/f_0 with ϕ is larger for smaller numbers of sides, as is the case for Q_0, which increases up to 30% at maximum tuning. This is related to the concentration of the field towards the vertexes: at angles different from 0, the gap between the external vertex and the face of the inner polygon increases for smaller number of sides, while the opposite holds for the gap between the midpoint of the external faces and the inner vertexes. This in turn leads to increased mode confinement, greater frequency shifts, and smaller surfaces for the mode currents to dissipate on.

TABLE I. Resonant frequency at $\phi = 0$ for different numbers of sides.

Side number	5	6	7	8	9
f_0 (GHz)	10.820	10.165	9.798	9.574	9.425

In the C factor plot we also include the results of driven modal simulations, which calculate modal S parameters and field profiles inside the cavity by driving the system through a lumped or wave port. In these simulations the port coupling was close to critical. As seen in Fig. 3(b), the two simulation approaches give different results for high tuning angles. The polygonal resonator can be seen as a cyclic concatenation of identical cavities or cells, and the overall system behavior depends on the coupling strength between adjacent cells. While in the case of strong coupling the complete system behaves as a single cavity, for couplings smaller than the mode linewidth the energy deposited in a cell will mostly be dissipated on its walls instead of being transmitted to the neighboring cells. As a consequence, a single antenna will not always be able to collect the entirety of the axion-deposited power, leading to a C factor reduction. This is not accounted for by eigenmode simulations, which mimic only the coherent excitation of all cells by the axion. On the other hand, driven modal simulations allow us to find the field distribution generated in the whole cavity excited by a single antenna, and, owing to electromagnetism's reciprocity, to gauge how much power is collected by it [45].

Mode crossings, i.e., regions where the axion-sensitive mode mixes with intruder modes, have been studied using driven modal simulations in the $N = 6$ case. The resulting transmission spectra are shown in Fig. 4. The map shows three groups of modes, each with four members that get closer in frequency at increasing tuning angles.

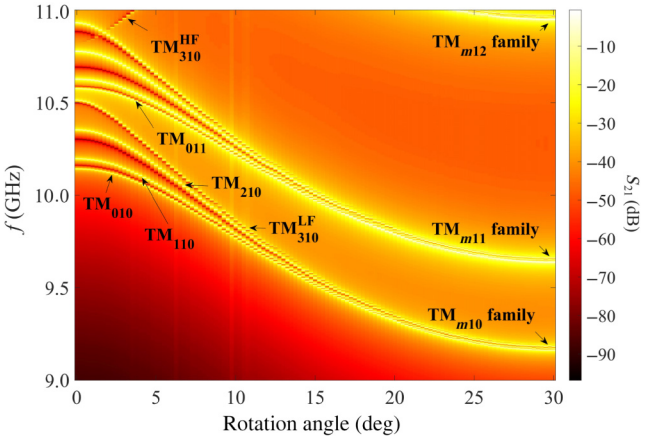

FIG. 4. Transmission S_{21} between two antennas on opposite endcaps as a function of tuning angle. A set of 121 driven modal simulations were performed setting copper conductivity at 4 K as boundary condition. For the axion-sensitive TM_{010} mode, the maximum frequency shift is about 1 GHz, with no mode mixing.

Focusing our attention on the group lowest in frequency, we identify its members as those originating from the (pseudo-)TM_{010}, TM_{110}, TM_{210}, and TM_{310} modes (see Appendix A) of the circular thin-shell cavity. However, the symmetry breaking caused by the shift to the polygonal model causes the angular degeneracy of the TM_{310} mode of the circular cavity to be lifted, separating the two modes into a low-frequency, vertex-centered TM^{LF}_{310} mode and a high-frequency, face-centered TM^{HF}_{310} mode. No mode crossings occur for the TM_{010} mode, which is always well coupled with the antennas. The studied mode is the fundamental TM one, so only crossings with TE and TEM modes would be possible. However, since the cavity has low aspect ratio, the frequency spacing of such intruder modes is large. Moreover, the employed dipole antennas would have extremely low coupling with intruder modes. In addition, we note that the separation between the studied mode and its neighbors exceeds their linewidths even at high tuning angles.

B. Study of allowed tolerances

Complex cavity designs are more likely susceptible to deviations from the ideal geometry. We evaluate the required mechanical tolerances needed in this geometry by considering horizontal misalignment and tilts between the two prisms at $\phi = 0$. Figure 5 reports the results for cavity parameters and figure of merit. We move the axis of the inner prism in the plane defined by the axis of the second prism and one of its vertexes. We separately study the effect of horizontal misalignment and of tilts about the center of the cavity.

The two datasets are presented in the same plot where the horizontal axis is the relative radial projection, i.e., the displacement of the intercept of the inner prism axis with the top endcap, normalized to the prisms' circumradius difference.

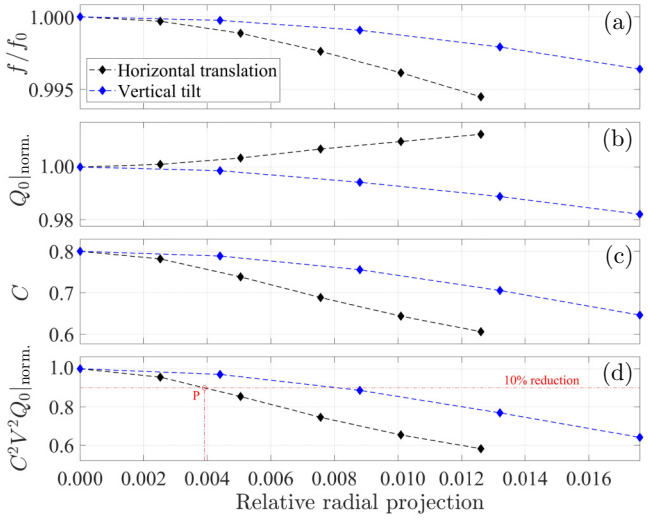

FIG. 5. Changes in the main cavity parameters due to varying degrees of reciprocal horizontal misalignment and tilting of the two prisms: (a) relative frequency shift, (b) normalized quality factor $Q_0|_{\text{norm.}}$, (c) C factor, and (d) normalized figure of merit. In the case of the 10-GHz cavity, the difference of the two circumradii is $d = 19.83$ mm, so the plot range corresponds to a lateral shift of $0.0176d \sim 349$ μm. The Q_0 of the unperturbed cavity was 62 000. In panel (d), point P indicates the earliest value at which the figure of merit reaches 90% of its maximum value, which happens for a translation of $0.0039d \sim 77.6$ μm.

Horizontal misalignments significantly impact the C factor and thus are the main source of cavity figure-of-merit degradation. Changes in quality factor and resonant frequency are much smaller. To limit the scan rate degradation due to horizontal translations within 10%, the minimum tolerance needed would be about 78 μm, within the capabilities of computerized numerical control machines.

III. EXPERIMENTAL RESULTS

A full-scale prototype of the cavity was obtained from bulk aluminum metal via single-pass wire electrodischarge machining and is shown in Fig. 6. The 420-mm-long cavity has r_{in} and r_{ext} of 55.91 and 39.14 mm, respectively. The longitudinal edges of the inner and outer prism are filleted with radii of 2 and 3 mm, respectively. In this prototype, the endcaps are divided into two pieces through a 50-μm-wide circular gap, allowing for rotation of the inner prism via a knob. Each endcap hosts eight apertures used for antenna insertion and dielectric bead pull characterization [46]. Of those, six were positioned to correspond to the outer prism vertexes, while the other two were in the middle of a side. All apertures were radially positioned to lie at the center of the cavity gap.

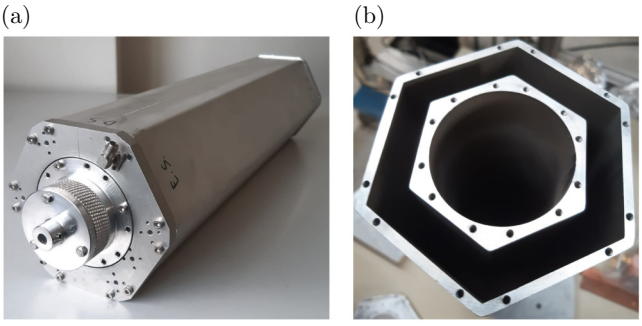

FIG. 6. The prototype hexagonal coaxial resonator: (a) external view; and (b) internal view.

The measured transmission spectrum of the cavity at $\phi = 0$ is shown in Fig. 7. The TM_{010} and TM_{011} modes are well isolated and the spectrum is clean before TM_{010}, in agreement with simulation results shown in Fig. 5. The frequency of the TM_{010} mode measured at room temperature was 10.1855 GHz, to be compared with 10.14 GHz yielded from numerical simulations. The measured quality factor was ∼4200, with negligible couplings on both antennas. In the $\phi = 0$ configuration, the field profiles and transmission spectra were independent of antenna positioning. The full tuning range for a rotation from 0 to $\phi_{\max}$ was about 1 GHz, as expected from simulations. Even though this cavity has a very high aspect ratio, no prominent mode mixings were noticed for the fundamental mode during tuning of the prototype, possibly as a consequence of coupling, positioning, and type of the employed antennas, or of overdamping of the intruder modes to the vacuum through the circular gaps in the endcaps.

Measurements of field profiles evidenced the presence of geometrical nonidealities. Figure 7 shows bead pull

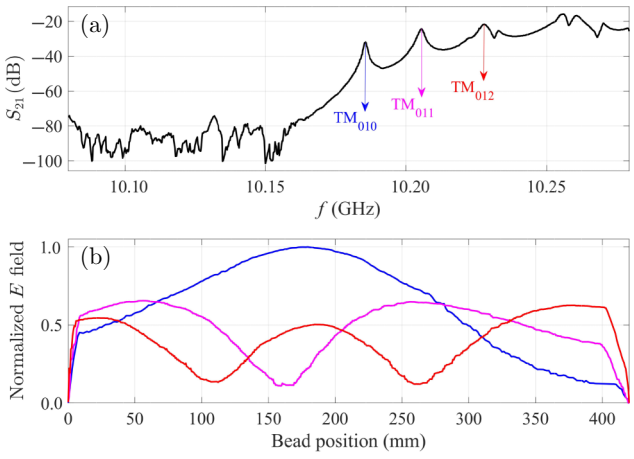

FIG. 7. Experimental results. (a) The transmission spectrum measured at $\phi = 0$, where we also indicate the position of the first three TM_{01n} modes. (b) The corresponding measured electric field profiles shown with the same colours.

results for the main mode and the two most adjacent ones. The TM_{010} mode longitudinal field profile peaks before the cavity center, and its magnitudes at the endcaps differ significantly. Marked asymmetries are also visible in the TM_{011} and TM_{012} modes. The cavity prototype is therefore longitudinally asymmetric. Concerning the azimuthal field distribution, we monitored the maximum field amplitudes for the TM_{010} mode, evidencing variations up to a factor 3. Numerical control machine measurements revealed deviations from design dimensions of up to a maximum of 0.14 mm. Minor geometry adjustments in the prism alignment resulted in a small frequency variation and no significant changes in the quality factor.

Subsequently, the cavity was internally coated with copper tape strips (see Appendix B), which improved the room-temperature Q_0 to 9400, to be compared with the value of 10 900 obtained for a bulk oxygen-free, high-conductivity copper cavity from simulations. Cooling to 77 K improved Q_0 to 17 800, smaller than the simulated value of 32 900. Among the possible reasons for this discrepancy may be a lower-than-expected improvement in rf conductivity for the copper tape, contact or radiative losses due to the presence of the circular gaps in the endcaps, contact losses in the endcaps with tape edges not always parallel to the direction of the current field of the mode, and finally additional geometrical nonidealities in the prototype induced by thermal contractions.

IV. CAVITY COMPARISONS

In Fig. 8 we report the overall figure of merit (FoM) F [see Eq. (3)] of the polygonal coaxial cavity for various magnet bore values. The working frequency has been set to 10 GHz and F is normalized to the value $F_c = 8.16 \times 10^{-3}$ m^6 obtained for a single cylindrical cavity of radius 11.48 mm and length 1 m resonating at the same frequency with $Q_0 = 100\,000$ and $C = 0.69$. For meaningful comparison, F is normalized to a cavity of unit length. For comparison, we also add the performances of some cavity setups described in the introduction: pizza cavities, cavity arrays, multirod cavities, dielectric photonic cavities, and wire metamaterial cavities. For a detailed breakdown of all the assumptions employed while compiling Fig. 8, refer to Appendix C.

In Fig. 8, we identify three regions of interest for high-frequency haloscopes. Below 80-mm-diameter magnet bore, the pizza cavity is the best approach, as arrays of cylindrical cavities have low tessellation efficiency. The performance of the present polygonal coaxial cavity is comparable to a pizza cavity using 5-mm-thick diaphragms (PC5 in Fig. 8). Between 80 and 120 mm, the polygonal cavity approach is a competitive solution for its higher simplicity compared to pizza cavities with 10–16 subdivisions and arrays of 5–11 cavities. In principle, arrays of cylindrical cavities would give the best figure of merit for bore

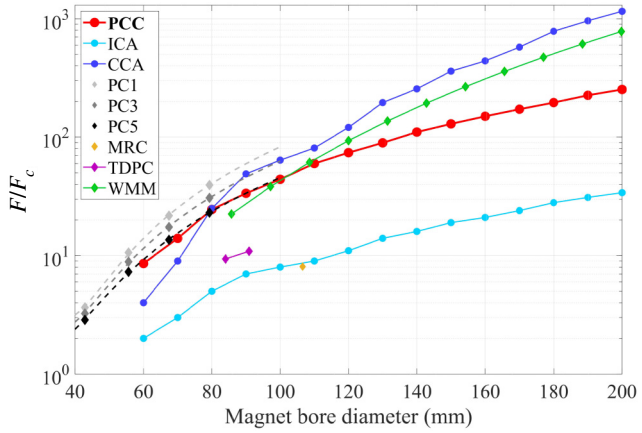

FIG. 8. Comparison between normalized figures of merit for different resonant cavity systems filling a magnet bore in a 10-GHz haloscope: PCC, polygonal coaxial cavity; ICA, independent cavity array; CCA, coherent cavity array; PC1, PC3, and PC5, pizza cavities employing diaphragms of 1, 3, and 5-mm thickness, respectively; MRC, multirod cavity; TDPC, tunable dielectric photonic cavity; WMM, wire metamaterial cavity. The corresponding dashed lines are second-order polynomial fits, while the solid lines represent only a guide to the eye.

magnets greater than ∼120 mm. However, one should be able to coherently read out a number of cavities ranging between 11 and 34, while the polygonal coaxial resonator is a practical solution. Moreover, multiple cavity arrays can be based also on nested polygonal coaxial cavities, greatly reducing the total number of cavities to be operated in parallel.

V. CONCLUSIONS

We introduced the tunable polygonal coaxial axion haloscope, and discussed it as a practical solution to the issue of the poor scaling of the scan rate with volume, particularly challenging in haloscopes in the range above ∼5 GHz. Compared to arrays of cavities, and the pizza cavity concept, this resonator presents a significant figure of merit and allows for a practical and effective tuning method by relative rotation of the internal prism with up to 5% tuning depth.

FEM simulations were employed to study relevant cavity parameters over the tuning range. No mode mixings were observed. We also estimated the required mechanical tolerances, which were found to be within the capabilities of commonly available numerical control machines.

A prototype aluminum hexagonal cavity was built and tested. The axion-sensitive mode was found near the expected frequency and was isolated for the full expected tuning range. Bead pull measurements were used to map the longitudinal field profiles and the azimuthal field distribution inside the resonator, showing unwanted asymmetries due to geometrical nonidealities of the prototype. More precise machining techniques, such as numerical control, will therefore be needed for future realizations.

The cavity's inner surfaces were covered with copper tape strips to increase its quality factor. At room temperature, this allowed us to reach $Q_0 \sim 10^4$, not far from the expected value. At liquid-nitrogen temperature, the measured Q_0 of the coated cavity was short of the simulated value for reasons not yet completely understood. Most likely, this is due to a limited rf low-temperature conductivity of the copper strips, or to variation of rf contact in the endcaps due to thermal contractions. The tuning mechanism should therefore be designed for cryogenic measurements, for instance, including ball-bearing guides. Flexible gaskets or quarter-lambda chokes should also be considered to ensure good rf connections.

In conclusion, the polygonal resonator represents an effective three-dimensional resonator for axion dark-matter haloscope searches at high frequency. Much higher quality factors up to the range of millions could be reached by coating the internal walls with high-temperature superconductor strips (see Ref. [47]). Additionally, even more efficient magnet bore occupation can be obtained by nested multiple polygonal coaxial cavities.

ACKNOWLEDGMENTS

This material in this paper was based upon work supported by INFN (QUAX experiment). We are grateful to E. Berto (University of Padova and INFN), who contributed substantially to the mechanical realization of this cavity. A. Benato, A. Pitacco, and M. Rebeschini of INFN Padova did part of the mechanical work and M. Zago (INFN) the mechanical drawings. The contributions of F. Calaon and M. Tessaro (INFN) to the measurement setup is gratefully acknowledged. The authors also thank A. Palmieri for useful discussions on the cavity concepts and M. Comunian for providing the server for FEM analysis.

APPENDIX A: ELECTRIC FIELD DISTRIBUTION FOR VARIOUS MODES AND TUNING VALUES

Figure 9 shows the electric field amplitude distributions obtained with driven modal simulations for the TM_{m10} modes found in Fig. 4. The antennas are positioned in the rightmost corner and the distributions are plotted in a transverse plane passing through the center of the cavity. Since we are using driven modal simulations, the plots allow us to visualize the cell decoupling phenomenon discussed in Sec. II A. For example, despite the TM_{010} mode being always free from mixing, the 30° plot shows a marked decrease in the field strength in the cavity regions further away from the two antennas. This field distribution corresponds to a decrease in C factor of about 60% when compared to the same cavity read out with an antenna array, as shown in Fig. 3. Mode mixing is instead observed at 30° between the TM_{110}, TM_{210}, and TM^{LF}_{310} modes,

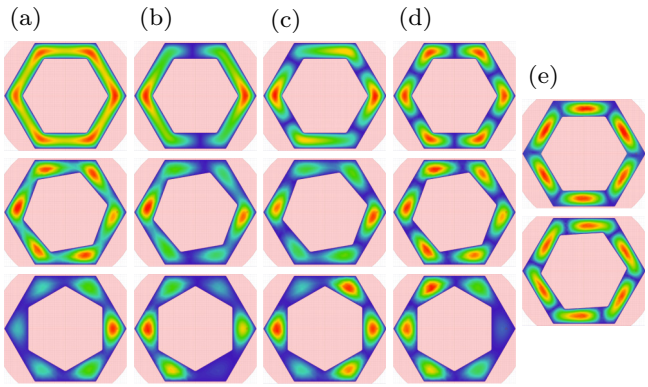

FIG. 9. Electric field distributions in a transverse section passing through the center of the cavity for the TM_{m10} modes found in Fig. 4: (a) TM_{010}, (b) TM_{110}, (c) TM_{210}, (d) TM_{310}^{LF}, and (e) TM_{310}^{HF}. All distributions have been normalized to their maximum amplitude (see color scale in Fig. 2). Each column represents the field distribution of a single mode at various tuning angles. For columns (a)–(d), the angles (from top to bottom) are 0°, 10°, and 30°. For column (e), the angles are 0.25° and 3.5°. The TM_{310}^{HF} mode is not visible at 0° due to null coupling with the antenna and also exits the observed frequency range after 3.5°.

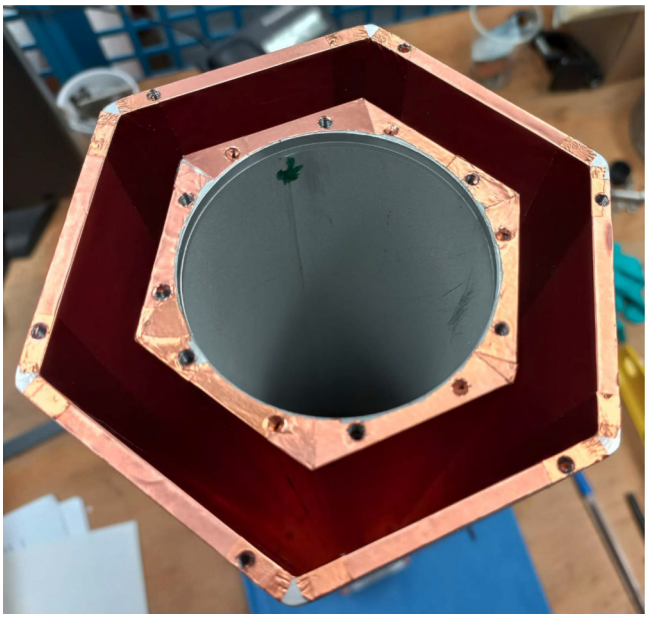

FIG. 10. The interior of the cavity after coating with copper tape strips.

due to their vicinity in frequency. Using the unperturbed field distributions at 10° and the polarity of the lobes (not represented in Fig. 9), it is possible to recognize the mode indicated with TM_{110} as an admixture of TM_{110} and TM_{210}, while the following two are respectively a sum and difference of TM_{210} and TM_{310}^{LF}.

APPENDIX B: THE COPPER-STRIP-COATED CAVITY

In Fig. 10, a photograph of the cavity after coating with copper strips is shown. The copper strips were contiguous sections of 30-μm-thick copper tape that were applied to the walls of the cavity longitudinally, so that they would be parallel to the direction of the currents for the TM_{010} mode. A small overlap between the tapes at the edges ensured that no part of the aluminum body was exposed to the inside volume. The strips were also applied on fixed endcaps for the cryogenic measurements, and for that reason tuning in this configuration was impossible.

APPENDIX C: ASSUMPTIONS EMPLOYED IN COMPILING FIG. 8

The following considerations have been made in constructing Fig. 8 in order to have all the cavities resonating at 10 GHz.

(1) For all cavities, an external wall thickness of 3 mm has been added to their nominal internal radius.

(2) We sometimes needed to rescale the FoM of cavities whose resonant frequency ν_c lies in the X band, but significantly differs from 10 GHz. In this case, we rescaled the section of the cavity by the inverse ratio of the frequency so that $V^2 \sim (\nu_c/10\ \mathrm{GHz})^4$. We additionally assumed that the surface conductivity is always determined in this region by the anomalous skin effect, so we rescaled their quality factor by $(\nu_c/10\ \mathrm{GHz})^{2/3}$ [48]. The equivalent FoM at 10 GHz is then given by the original FoM multiplied by a scaling factor of $(\nu_c/10\ \mathrm{GHz})^{-14/3}$. The obtained value is then associated in the graph to a magnet bore value corresponding to the rescaled cavity radius. Note that this procedure is not applicable to cavities in which dielectric losses substantially impact the Q factor.

(3) *Polygonal coaxial cavity.* To fix the TM_{010} frequency at 10 GHz, the gap thickness is kept constant for increasing magnet bore, while the number of sides is qualitatively scaled as the square root of the magnet bore. The external radius is adjusted to the maximum possible value. The C factor is 0.8 and we use a conservative value of 50 000 for the quality factor.

(4) *Pizza cavities.* Calculated values are based on published data [33] obtained for cavities with two, four, six, and eight sections. The original values from Table 3 in Ref. [33] have been rescaled as previously described for the comparison at 10 GHz. We used an approximate value of $C = 0.65$ for all cavities.

(5) *Cavity arrays.* Multiple cylindrical cavities are arranged to optimally fill the available volume. Arrays of two to 34 cavities can be hosted within the bore. Note that, as a consequence of the normalization, the normalized factor of merit is simply K and K^2 in the case of independently and coherently read cavity arrays, respectively.

(6) *Multirod cavity.* We consider the cavities described in Ref. [22] and with more detail in Ref. [49]. Each cavity design appearing in Fig. 4.2(a) of the latter was normalized to work at 10 GHz. The resulting best FoM is reported in Fig. 8.

(7) *Tunable dielectric photonic cavity.* We use the experimental measurements at cryogenic temperatures reported in Fig. 10 of Ref. [29]. The cavity consisted of a 78-mm-diameter, 100-mm-long copper cylinder containing nine 9-mm-thick alumina poles which extended through slots in both endcaps. Four pairs of 7-mm-thick copper poles were also employed to constrain the cavity field. The frequency of 10 GHz is reached by this resonator at the middle of its tuning range, but the maximum normalized FoM is reached at the highest operating frequency of 10.89 GHz. For this reason, in Fig. 8 we report both values, with the point at 84 mm corresponding to the non-normalized values obtained at 10 GHz and the point at 90.9 mm corresponding to the rescaled ones obtained at 10.89 GHz [50]

(8) *Plasma haloscope.* We refer to the projections in Ref. [32]. With an excess approximation, we assume that optimal filling of a circular section does not significantly impact the C and Q factors if compared to those obtained for a square section. Consequently, an unloaded Q factor of 21 400 is deduced from Fig. 4 of Ref. [32], and a value of 0.6 is used for C. We assume an interwire distance of 11.4 mm and correct the total internal volume by a factor of $\sim$0.975 as is the case for an array of 2-mm-diameter wires.

[1] S. Weinberg, A new light boson? Phys. Rev. Lett. **40**, 223 (1978).

[2] F. Wilczek, Problem of strong P and T invariance in the presence of instantons, Phys. Rev. Lett. **40**, 279 (1978).

[3] R. D. Peccei and H. R. Quinn, CP conservation in the presence of pseudoparticles, Phys. Rev. Lett. **38**, 1440 (1977).

[4] R. D. Peccei and H. R. Quinn, Constraints imposed by CP conservation in the presence of pseudoparticles, Phys. Rev. D **16**, 1791 (1977).

[5] I. G. Irastorza and J. Redondo, New experimental approaches in the search for axion-like particles, Prog. Part. Nucl. Phys. **102**, 89 (2018).

[6] R. Workman, V. Burkert, V. Crede, E. Klempt, U. Thoma, L. Tiator, K. Agashe, G. Aielli, B. Allanach, C. Amsler, *et al.*, Review of particle physics, Prog. Theor. Exp. Phys. **2022**, 083C01 (2022).

[7] A. Caputo and G. Raffelt, in *Proceedings of 1st General Meeting and 1st Training School of the COST Action COSMIC WISPers – PoS(COSMICWISPers)* (2024), Vol. 454, p. 041.

[8] M. Buschmann, J. W. Foster, A. Hook, A. Peterson, D. E. Willcox, W. Zhang, and B. R. Safdi, Dark matter from axion strings with adaptive mesh refinement, Nat. Commun. **13**, 1049 (2022).

[9] P. Sikivie, Experimental tests of the "invisible" axion, Phys. Rev. Lett. **51**, 1415 (1983).

[10] M. S. Turner, Periodic signatures for the detection of cosmic axions, Phys. Rev. D **42**, 3572 (1990).

[11] B. M. Brubaker, L. Zhong, S. K. Lamoreaux, K. W. Lehnert, and K. A. van Bibber, HAYSTAC axion search analysis procedure, Phys. Rev. D **96**, 123008 (2017).

[12] D. Kim, J. Jeong, S. Youn, Y. Kim, and Y. K. Semertzidis, Revisiting the detection rate for axion haloscopes, arXiv:2001.05605 [hep-ex].

[13] W. U. Wuensch, S. De Panfilis-Wuensch, Y. K. Semertzidis, J. T. Rogers, A. C. Melissinos, H. J. Halama, B. E. Moskowitz, A. G. Prodell, W. B. Fowler, and F. A. Nezrick, Results of a laboratory search for cosmic axions and other weakly coupled light particles, Phys. Rev. D **40**, 3153 (1989).

[14] C. Hagmann, P. Sikivie, N. S. Sullivan, and D. B. Tanner, Results from a search for cosmic axions, Phys. Rev. D **42**, 1297 (1990).

[15] C. Bartram, T. Braine, R. Cervantes, N. Crisosto, N. Du, G. Leum, L. Rosenberg, G. Rybka, J. Yang, D. Bowring, *et al.*, Axion dark matter experiment: Run 1B analysis details, Phys. Rev. D **103**, 032002 (2021).

[16] C. Bartram, T. Braine, E. Burns, R. Cervantes, N. Crisosto, N. Du, H. Korandla, G. Leum, P. Mohapatra, T. Nitta, *et al.*, Search for invisible axion dark matter in the 3.3–4.2 μeV mass range, Phys. Rev. Lett. **127**, 261803 (2021).

[17] M. Jewell, A. Leder, K. Backes, X. Bai, K. van Bibber, B. Brubaker, S. Cahn, A. Droster, M. H. Esmat, S. Ghosh, *et al.*, New results from HAYSTAC's phase II operation with a squeezed state receiver, Phys. Rev. D **107**, 072007 (2023).

[18] A. K. Yi, S. Ahn, Ç. Kutlu, J. Kim, B. R. Ko, B. I. Ivanov, H. Byun, A. F. Van Loo, S. Park, J. Jeong, *et al.*, Axion dark matter search around 4.55 μeV with Dine-Fischler-Srednicki-Zhitnitskii sensitivity, Phys. Rev. Lett. **130**, 071002 (2023).

[19] R. Di Vora, A. Lombardi, A. Ortolan, R. Pengo, G. Ruoso, C. Braggio, G. Carugno, L. Taffarello, G. Cappelli, N. Crescini, *et al.*, Search for galactic axions with a traveling wave parametric amplifier, Phys. Rev. D **108**, 062005 (2023).

[20] H. Chang, J.-Y. Chang, Y.-C. Chang, Y.-H. Chang, Y.-H. Chang, C.-H. Chen, C.-F. Chen, K.-Y. Chen, Y.-F. Chen, W.-Y. Chiang, *et al.*, First results from the Taiwan Axion Search Experiment with a haloscope at 19.6 μeV, Phys. Rev. Lett. **129**, 111802 (2022).

[21] I. Stern, A. A. Chisholm, J. Hoskins, P. Sikivie, N. S. Sullivan, D. B. Tanner, G. Carosi, and K. van Bibber, Cavity design for high-frequency axion dark matter detectors, Rev. Sci. Instrum. **86**, 123305 (2015).

[22] M. Simanovskaia, A. Droster, H. Jackson, I. Urdinaran, and K. van Bibber, A symmetric multi-rod tunable microwave cavity for a microwave cavity dark matter axion search, Rev. Sci. Instrum. **92**, 033305 (2021).

[23] B. T. McAllister, G. Flower, L. E. Tobar, and M. E. Tobar, Tunable supermode dielectric resonators for axion dark-matter haloscopes, Phys. Rev. Appl. **9**, 014028 (2018).

[24] A. P. Quiskamp, B. T. McAllister, G. Rybka, and M. E. Tobar, Dielectric-boosted sensitivity to cylindrical

azimuthally varying transverse-magnetic resonant modes in an axion haloscope, Phys. Rev. Appl. **14**, 044051 (2020).

[25] J. Kim, S. Youn, J. Jeong, W. Chung, O. Kwon, and Y. K. Semertzidis, Exploiting higher-order resonant modes for axion haloscopes, J. Phys. G **47**, 035203 (2020).

[26] D. Alesini, C. Braggio, G. Carugno, N. Crescini, D. D'Agostino, D. Di Gioacchino, R. Di Vora, P. Falferi, U. Gambardella, C. Gatti, *et al.*, Realization of a high quality factor resonator with hollow dielectric cylinders for axion searches, Nucl. Instrum. Meth. A **985**, 164641 (2021).

[27] R. Di Vora, D. Alesini, C. Braggio, G. Carugno, N. Crescini, D. D'Agostino, D. Di Gioacchino, P. Falferi, U. Gambardella, C. Gatti, *et al.*, High-Q microwave dielectric resonator for axion dark-matter haloscopes, Phys. Rev. Appl. **17**, 054013 (2022).

[28] D. Alesini, C. Braggio, G. Carugno, N. Crescini, D. D'Agostino, D. Di Gioacchino, R. Di Vora, P. Falferi, U. Gambardella, C. Gatti, *et al.*, High quality factor photonic cavity for dark matter axion searches, Rev. Sci. Instrum. **91**, 094701 (2020).

[29] S. Bae, S. Youn, and J. Jeong, Tunable photonic crystal haloscope for high-mass axion searches, Phys. Rev. D **107**, 015012 (2023).

[30] Y. Kishimoto, Y. Suzuki, I. Ogawa, Y. Mori, and M. Yamashita, Development of a cavity with photonic crystal structure for axion searches, Prog. Theor. Exp. Phys. **2021**, 063H01 (2021).

[31] M. Lawson, A. J. Millar, M. Pancaldi, E. Vitagliano, and F. Wilczek, Tunable axion plasma haloscopes, Phys. Rev. Lett. **123**, 141802 (2019).

[32] A. J. Millar, S. M. Anlage, R. Balafendiev, P. Belov, K. Van Bibber, J. Conrad, M. Demarteau, A. Droster, K. Dunne, A. G. Rosso, *et al.*, Searching for dark matter with plasma haloscopes, Phys. Rev. D **107**, 055013 (2023).

[33] J. Jeong, S. Youn, S. Ahn, J. E. Kim, and Y. K. Semertzidis, Concept of multiple-cell cavity for axion dark matter search, Phys. Lett. B **777**, 412 (2018).

[34] J. Jeong, S. Youn, and J. E. Kim, Multiple-cell cavity design for high mass axion searches: An extended study, Nucl. Instrum. Meth. A **1053**, 168327 (2023).

[35] A. Á. Melcón, S. A. Cuendis, C. Cogollos, A. Díaz-Morcillo, B. Döbrich, J. D. Gallego, J. Barceló, B. Gimeno, J. Golm, I. G. Irastorza, *et al.*, Scalable haloscopes for axion dark matter detection in the 30 μeV range with RADES, J. High Energy Phys. **2020**, 1 (2020).

[36] C. Hagmann, P. Sikivie, N. Sullivan, D. B. Tanner, and S. Cho, Cavity design for a cosmic axion detector, Rev. Sci. Instrum. **61**, 1076 (1990).

[37] D. S. Kinion, First results from a multiple microwave cavity search for dark matter axions, Ph.D. thesis, University of California, Davis, 2001.

[38] J. Yang, J. R. Gleason, S. Jois, I. Stern, P. Sikivie, N. S. Sullivan, and D. B. Tanner, Search for 5–9 μeV axions with ADMX four-cavity array, Springer Proc. Phys. **245**, 53 (2020).

[39] C. Adair, K. Altenmüller, V. Anastassopoulos, S. Arguedas Cuendis, J. Baier, K. Barth, A. Belov, D. Bozicevic, H. Bräuninger, G. Cantatore, *et al.*, Search for dark matter axions with CAST-CAPP, Nat. Commun. **13**, 6180 (2022).

[40] J. Jeong, S. Youn, S. Ahn, C. Kang, and Y. K. Semertzidis, Phase-matching of multiple-cavity detectors for dark matter axion search, Astropart. Phys. **97**, 33 (2018).

[41] C.-L. Kuo, Large-volume centimeter-wave cavities for axion searches, arXiv:1910.04156 [physics.ins-det].

[42] C.-L. Kuo, Symmetrically tuned large-volume conic shell-cavities for axion searches, arXiv:2010.04337 [physics.ins-det].

[43] T. A. Dyson, C. L. Bartram, A. Davidson, J. B. Ezekiel, L. M. Futamura, T. Liu, and C.-L. Kuo, High-volume tunable resonator for axion searches above 7 GHz, Phys. Rev. Appl. **21**, L041002 (2024).

[44] R. Bradley, J. Clarke, D. Kinion, L. J. Rosenberg, K. van Bibber, S. Matsuki, M. Mück, and P. Sikivie, Microwave cavity searches for dark-matter axions, Rev. Mod. Phys. **75**, 777 (2003).

[45] Nonetheless, provided each cell has its own tunable antenna, the present polygonal resonator becomes a cavity array in which the multiple cavities have $C \sim 0.6$, $Q \sim$ 60,000, and are all tuned together over a large range. In addition, for phase-matched readout, the cavity cells would only need an additional fine-tuning mechanism to compensate for small frequency differences between cells. Note that when phase matching is employed, the form factor calculated from the eigenmode simulations is recovered.

[46] S. Som, S. Seth, A. Mandal, and S. Ghosh, Bead-pull measurement using phase-shift technique in multi-cell elliptical cavity, Proc. IPAC **280**, 2011 (2011).

[47] D. Ahn, O. Kwon, W. Chung, W. Jang, D. Lee, J. Lee, S. W. Youn, H. Byun, D. Youm, and Y. K. Semertzidis, Biaxially textured $YBa_2Cu_3O_{7-x}$ microwave cavity in a high magnetic field for a dark-matter axion search, Phys. Rev. Appl. **17**, L061005 (2022).

[48] A. Vagov, I. A. Larkin, M. D. Croitoru, and V. M. Axt, Superanomalous skin-effect and enhanced absorption of light scattered on conductive media, Sci. Rep. **13**, 5103 (2023).

[49] M. Simanovskaia, Design, Fabrication, and Characterization of a High-Frequency Microwave Cavity for HAYSTAC, Ph.D. thesis, University of California, Berkeley, 2020.

[50] Note that, while the cavity contains dielectrics, we are allowed on first approximation to apply the renormalization procedure since we can ascertain from the data in Table II of Ref. [29] that at cryogenic temperatures the contribution to the losses of the dielectrics is of the order of 5%.